Materials Chemistry and Physics 344 (2025) 131101

Contents lists available at ScienceDirect

Materials Chemistry and Physics

journal homepage: www.elsevier.com/locate/matchemphys

Formation and magnetic behaviour of nanostructured Fe nanomesh prepared on porous alumina surface

D.I. Tishkevich [a,*], A.I. Vorobjova [b], E.A. Outkina [b], S.M. Zavadskii [b], I.U. Razanau [a], T.I. Zubar [a], A.A. Bondaruk [a], A.A. Rotkovich [a], M.I. Sayyed [c,d], M.V. Silibin [e,f], A. Yu Gerasimenko [e], O.A. Sycheva [g], S.V. Trukhanov [a], A.V. Trukhanov [a]

[a] SSPA "Scientific-Practical Materials Research Centre of NAS of Belarus", 220072, Minsk, Belarus
[b] Micro- and Nanoelectronics Department, Belarusian State University of Informatics and Radioelectronics, 220013, Minsk, Belarus
[c] Renewable Energy and Environmental Technology Center, University of Tabuk, Tabuk, 47913, Saudi Arabia
[d] Department of Physics, Faculty of Science, Isra University, 1162, Amman, Jordan
[e] Institute for Advanced Materials and Technologies, National Research University of Electronic Technology "MIET", Zelenograd, Moscow, 124498, Russia
[f] I.M. Sechenov First Moscow State Medical University, Moscow, 119435, Russia
[g] Institute of General and Inorganic Chemistry, National Academy of Sciences of Belarus, Minsk, 220072, Belarus

HIGHLIGHTS

- A detailed description of the nanoporous Fe films on the PAA membrane surface is presented.
- Magnetic measurements revealed that Fe films are characterized by perpendicular magnetic anisotropy.
- Fe-PAA nanocomposite has thermal stability for a temperature up to 600 °C.
- Fe-PAA composite can be used as magnetically sensitive transistors, magnonic crystals, and heat-resistant sensitive sensors.

ARTICLE INFO

Keywords:
Magnetic nanoparticles
Nanoporous iron films
Porous alumina membrane
Film nanostructures
Magnetic anisotropy

ABSTRACT

The process for the preparation of nanoporous Fe films on the surface of a porous anodic alumina (PAA) membrane (with pore diameters of 50, 65, and 80 nm) is performed. PAA membranes with different topological parameters are used as a base with a relief porous surface on which Fe films with a thickness of up to 95 ± 5 nm are deposited by ion beam evaporation. The morphology of the Fe films completely replicates the relief of the porous membranes, as shown by the electron microscopy with element analysis. Fe films are uniformly deposited on the surface of PAA cells around the pores and represent a cellular-porous hexagonally ordered Fe array nanostructure. The results of the magnetic measurements show that the Fe films are characterized by perpendicular magnetic anisotropy with a twofold increase in the coercive force when measured in the perpendicular geometry compared to the in-plane direction. The obtained results show the possibility of wide practical application of such Fe films: for the fabrication of magnetically sensitive transistors, magnonic crystals, as a material for nanoelectrodes for studying electrochemical processes in the nanometer range and heat-resistant magnetically sensitive sensors.

1. Introduction

In the middle of the last century, a field of scientific knowledge emerged that was dedicated to the study of macroscopic ensembles of nanoparticles (1–100 nm size) and the physics of ultradisperse media [1]. This size range ensures good dimensional compatibility with the size of genes (width 2 nm and length 10–100 nm), proteins (5–50 nm), and viruses (2–400 nm) [2]. The biomedical applications of magnetic nanoparticles (MNPs) are of special interest. For example, highly sensitive disease diagnostics and precise targeted drug delivery (biomedical devices). The increased interest in nanoparticles of magnetic Fe, Ni, Co, and their chemical compounds is also determined by the potential

* Corresponding author.
E-mail address: dashachushkova@gmail.com (D.I. Tishkevich).

https://doi.org/10.1016/j.matchemphys.2025.131101
Received 11 February 2025; Received in revised form 8 May 2025; Accepted 28 May 2025
Available online 29 May 2025

possibilities of their use for creating magnetic memory with a high recording density and new generation electronic devices: magneto-sensitive transistors [3], sensor devices [4], and magnonic crystals [5–7].

The most widely studied MNPs with respect to biomedical applications are Fe, magnetite (Fe_3O_4), and maghemite (γ-Fe_2O_3) MNPs [6–8]. Compared to pure metals and most magnetic alloys, iron oxide nanoparticles are less toxic [9,10]. Statistical data indicate that about 92 % of iron oxide-based MNPs are obtained by chemical methods, while physical and biological synthesis methods are used in 6 % and 2 % of the cases, respectively [11,12]. At the same time, the physical synthesis of MNPs has attracted a great deal of interest in recent years, because these methods enable the large-scale production of nanoparticles.

Among the innovative strategies for the production of large batches of nanoparticles, the idea of forming arrays of nanostructures is attracting attention. The arrays can be based on different nanoparticle shapes: nanopillars, nanowires, nanotubes, and nanomesh [13–18]. One of the possible directions in the study of such arrays is the synthesis and study of porous films in the form of an ordered network of nanopores ("antidots") that exhibit the property of perpendicular magnetic anisotropy (PMA), since they can be used as media for creating new types of sensors and biochemical control devices [19,20]. The formation of the upper electrode of the sensor in the form of a nanoporous structure with a given pore size makes it possible to achieve the required level of selectivity while eliminating the adsorption of interfering components on the sensitive layer [21]. Currently, planar electrodes of such sensors are made from gold, platinum or graphite using photolithographic methods [22,23]. An ordered arrays of magnetic "antidots" (porous magnetic films in the form of an ordered network of nanopores) can also be formed by nanopatterning continuous films using various lithographic methods [24,25]. However, a simpler and more economical way of their formation is the deposition of magnetoanisotropic films on various porous templates [26,27]. Typically, polycarbonate and porous anodic alumina-based membranes are used for these purposes [28–30].

Porous anodic aluminum oxide (PAA) constantly attracts the attention of scientists due to its unique ordered honeycomb structure of cells. This structure allows the formation of many new micro- and nanoelements by the template synthesis method [31–33] and is also an indispensable medium for conducting unique scientific research on nanocrystalline functional and nanocomposite materials with grain sizes less than 100 nm. The use of the PAA expands the possibilities for creating a new generation of composite materials and films with low specific gravity and thickness with high values of thermomechanical resistance at operating temperatures up to 800 °C.

All over the world, active research is being conducted into nanocomposite materials for use in biotechnological and medical developments: for the separation of organic macromolecules and proteins (biofiltration), in biosensor devices, in capsule (from PAA) drug delivery systems, for implants coating, as a base for the formation of biocompatible tissues, etc. [32,34–36]. Applications of nanocomposite magnetic materials are especially numerous in medicine: magnetic resonance imaging, magnetic hyperthermia and thermal ablation, magnetic targeted therapy and drug delivery, magnetic separation, relaxometry, regenerative medicine, magnetic biodetection, etc. [37–39]. The composite material that we have fabricated and studied (nanoporous Fe films on PAA surface membranes) is supposed to be used in the development of heat-resistant magnetically sensitive electrodes of sensors.

The development of sensors with high sensitivity and selectivity with minimal energy consumption on a substrate based on PAA in combination with a new magnetic material of the sensitive layer (nanoporous Fe films) is an urgent task. This will allow to obtain energy-efficient sensors (in an integrated design) with sensitive elements made of porous magnetic films on a substrate of nanostructured PAA. For this purpose, sensor designs in the form of interdigital electrodes can be used or with two sensitive elements and a common power source on a single dielectric substrate to increase selectivity and reduce power consumption [40,41]. An analysis of examples of magnetic biodetection [42,43] also made it possible to evaluate the prospects for creating from this Fe-PAA nanocomposite material for film detectors based on the giant magnetoimpedance effect (GME) for bioapplications, with the aim of continuing research.

Due to the unique structure of PAA, it is an almost ideal template. Its cylindrical pores form an ordered matrix normal to the surface. The ability to control the structure by adjusting the anodization duration and voltage, the nature and composition of the electrolyte is another advantage of these matrices [44–46].

In our previous works, we have studied the processes of formation of arrays of nanopillars, nanowires, and nanotubes in the pores of PAA using electrochemical methods [47–49]. In this work, we present the results of a study of the synthesis process of Fe nanoporous films not in the bulk but on the surface of PAA. Nucleation and growth into nano-sized Fe arrays is achieved using the specific surface areas of the PAA templates. A PAA membrane is used as a base with a relief porous surface on which thin Fe films with a thickness of up to 100 nm are deposited by means of ion beam evaporation. As a result, a nanoporous Fe magnetic film is formed on the surface of the PAA. The film can also be described as a mesh of nanosized thickness with nanosized geometric parameters (pores) corresponding to the parameters of the PAA.

The study of the physical properties of thin nanoporous magnetic films (with pore diameters in the range of 10–200 nm) is an urgent task from both fundamental and practical points of view. The relevance of basic research on such materials is explained by their fundamentally new properties, the physical nature of which is related to surface, dimensional, and quantum effects. The unique controlled magnetic properties of nanoporous magnetic films provide opportunities for their wide practical application [50]. Fabricating magnetic films by depositing them onto porous templates, such as PAA templates, will significantly simplify the production of such materials and reduce its cost compared to traditional lithographic methods.

The aim of this work is to obtain nanoporous Fe films on PAA surface with different topological parameters and to study the morphological, structural, and magnetic properties of the obtained nanocomposite material for use as a sensitive layer in heat-resistant magnetic sensors.

2. Materials and methods

2.1. Samples preparation

2.1.1. PAA template preparation

In many works, off-the-shelf industrially produced PAA membranes are used to produce samples ranging in size from micrometers to millimeters (up to 25 mm) [20,51]. Commercial alumina templates from Whatman plc© "Anodisc™ 25" have three nominal pore sizes: 20, 100, and 200 nm and are designated NCA20, NCA100, and NCA200, respectively [52]. In-house fabrication of PAA is used when large-area samples with varying pore sizes and a uniform pore distribution are required [53–55].

In this study, a two-step potentiostatic anodization was used to prepare the membranes of 3.3 ± 0.2 μm thickness. The membranes were fabricated from 99.9994 Al foil with a thickness of ~100 μm at anodizing voltages of (40, 50, and 60) ±2 V in an aqueous solution of oxalic acid (4 % $C_2H_2O_4$) at 15 °C. As a result, a PAA template with an ordered structure (Fig. 1) with different pore diameters and a thickness of 3.3 ± 0.2 μm was obtained. SEM images of the self-made PAA template after etching the Al substrate are shown in Fig. 1. Three types of PAA samples of 3.3 ± 0.2 μm thickness with varying pore diameters and the distance between their centers were fabricated: sample type I (anodizing voltage 40 ± 2 V), sample type II (anodizing voltage 50 ± 2 V), and sample type III (anodizing voltage 60 ± 2 V).

The maximum membrane area can be as large as (48 × 60) mm or (70 × 70) mm, the glass ceramic substrate standard size. Either side of

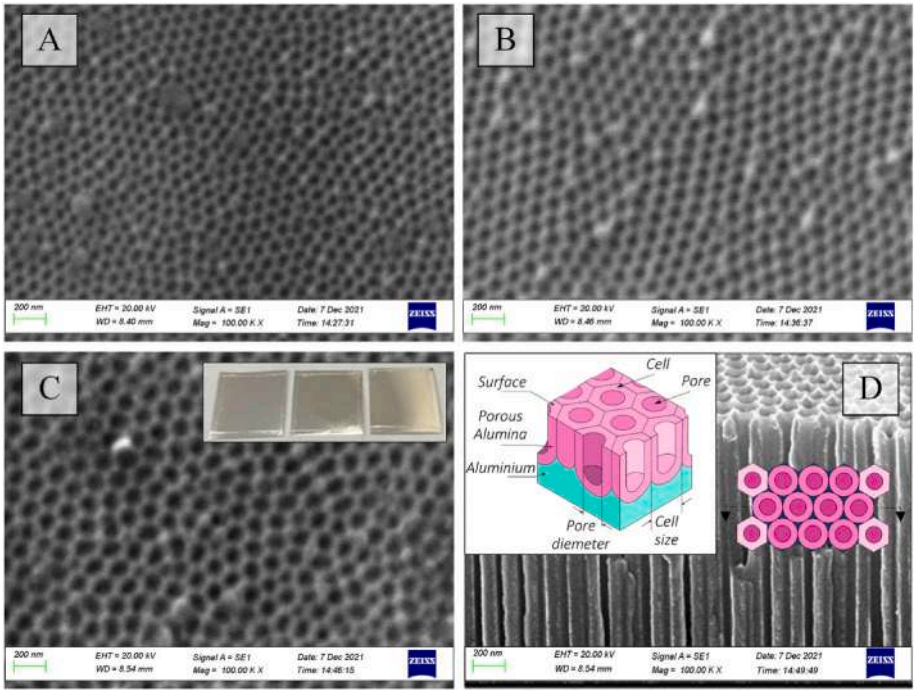

Fig. 1. SEM images of the as-prepared samples of PAA membrane with size of (15 × 15 mm) and thickness of 3.3 ± 0.2 μm with different pore diameters: A, B, C – samples of types I, II, and III, respectively, D – schematic representation of the cross-section and surface of the PAA template.

such a membrane can be coated by thin metal films using standard vacuum equipment and tools. The manufacturing process of such PAAs is described in more detail in previously published works [56,57].

2.1.2. The process of the Fe deposition

Ferromagnetic metal (Fe) was deposited by ion-beam evaporation using a VU2M vacuum setup under the following conditions: pressure in the vacuum chamber — $2{\cdot}10^{-2}$ Pa, substrate temperature — 303–313 K, deposition rate — 0.2 nm/s. The thickness of the deposited Fe under given deposition conditions is linearly proportional to the deposition time. An iron target with 99.995 % purity was used. The PAA templates were cleaned by Ar ion bombardment prior to Fe deposition. The studies were carried out for two Fe film thicknesses: 30 and 95 ± 5 nm. Typically, when atoms are deposited by vacuum evaporation directly onto a solid surface, in this case PAA, they gradually stack up to form islands and then continuous films [26,46]. The nucleation and accumulation of Fe atoms occurs in certain areas of the PAA surface (in the area of PAA cells around the pores, inset in Fig. 1 D) with the formation of porous nanosized Fe meshes.

2.2. Samples characterization

Surface topography and microstructure of the samples were studied by scanning electron microscopy (SEM) in both top and cross-sectional views using a Carl Ziess EVO-10 scanning electron microscope with an Oxford energy-dispersive X-ray detector (EDX).

The crystal structure of Fe MNPs was studied at room temperature by X-ray diffraction (XRD) method using a POWDIX 600/300 diffractometer with CuKα radiation ($\lambda = 0.154242$ nm). The acquisition time was $\Delta t = 3$ s. Measurements were performed with the step of 0.03°, in some cases 0.01°.

A Liquid Helium Free High Field Measurement System [58] was used to measure the magnetic parameters of the samples by vibration magnetometry. The temperature range of the measurement was 4.2–300 K. The applied magnetic field was ±2 T.

Differential thermal analysis (DTA) and thermogravimetric analysis (TGA) of the Fe-PAA samples were performed using a synchronous thermal analyzer NETZSCH STA 409 PC/PG Luxx (Germany) with vertical loading of samples. A sample with weight of 30–50 mg was placed in an open-type Allundum crucible. Measurements were performed in a dynamic air atmosphere (air flow rate 50 ml/min, protective gas – argon). Temperature range was from room temperature to 700 °C, heating rates were 10 ÷ 20 °C/min.

3. Results and discussion

3.1. Morphology of the Fe-PAA samples

Three types of PAA samples of 3.3 ± 0.2 μm thickness with different pore diameters were fabricated (Fig. 1). After each major step of the PAA production process, the samples were examined by SEM (Table 1 and Fig. 2).

The pore diameter for the PAA (d) is linearly proportional to the anodizing voltage U with a proportionality constant λ_p of approximately 1.29 nm × V^{-1} [59]:

$$d = \lambda_p \times U \quad (1)$$

where d – a pore diameter (nm).

Table 1
The main morphological characteristics of the experimental samples (as-fabricated amorphous PAA).

Type of sample	Anodizing voltage U, V	Diameter of pores d, nm	Porosity α, %	Diameter of cell D, nm
I	40	51.6[a] (51 ± 5)	17	100[a] (105 ± 5)
II	50	64.5[a] (68 ± 5)	23	125[a] (130 ± 5)
III	60	77.4[a] (81 ± 5)	27	150[a] (160 ± 5)

[a] The calculated values, the values in brackets are mean values measured by SEM.

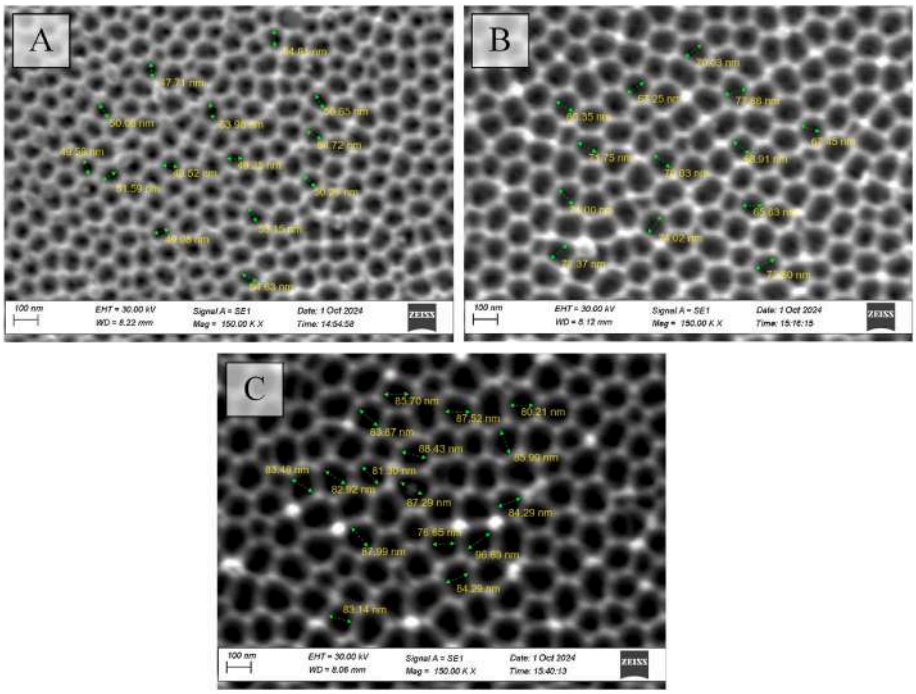

Fig. 2. SEM images of outer surfaces as-fabricated samples No. I (A), II (B), and III (C).

U – an anodizing voltage (V).

Interpore distance (cell diameter) of PAA (D) is linearly proportional to the anodizing voltage at the steady-state growth of PAA with a proportionality constant λ_c of approximately 2.5 nm × V^{-1} [60]:

$$D = \lambda_c \times U \quad (2)$$

The alumina porosity (α) was determined by formulas given in Ref. [61].

Fig. 2 demonstrates the SEM views of the outer surface of as-fabricated samples No. I, II, III.

Fig. 3 shows the SEM images of the template samples with the deposited Fe film. The thickness of the Fe film is 95 ± 5 nm. Unfortunately, it was not possible to determine the uniformity or to see the morphological defects of the Fe film at this magnification. Comparison of the SEM images shown in Figs. 1–3 does not allow visual

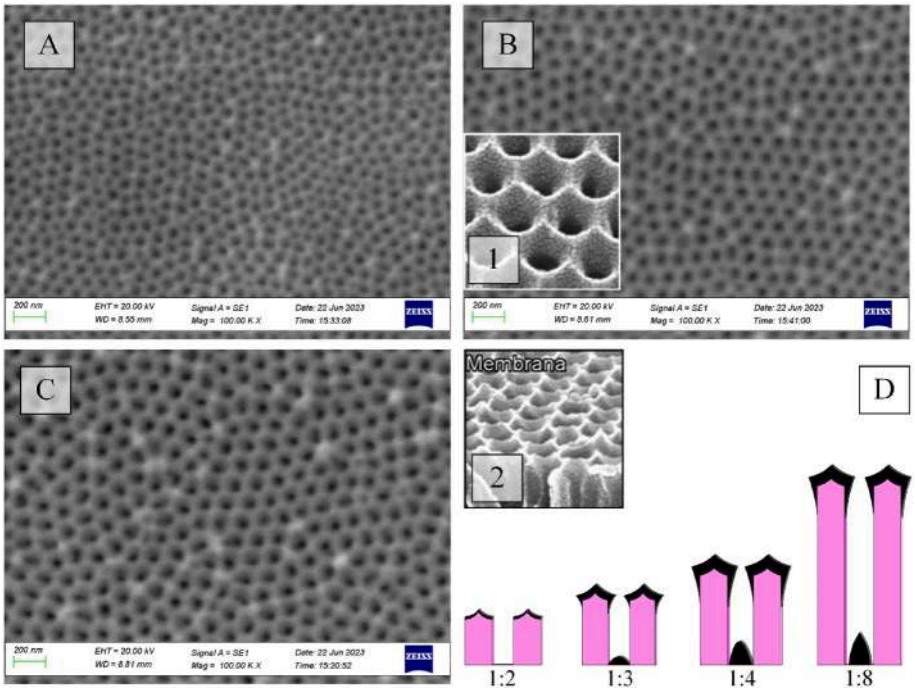

Fig. 3. SEM images of the surface of the Fe-PAA samples with a 95 ± 5 nm thick Fe film: A, B, C – samples of types I, II, and III, respectively, D – theoretical diagram, explaining how metal is deposited on the surface of a porous alumina of different thicknesses from Ref. [62]. The insets show fragments of the membrane surface before metal deposition.

determination of the locations where Fe is deposited on the surface of PAA membranes. One can only assume that deposition occurs in the region of the PAA cells around the pores and possibly in the oxide pores, as schematically shown in Fig. 3D, and that a cellular-porous hexagonally ordered nanostructure is formed.

In our case, the thickness of the deposited Fe film is very small, ~95 ± 5 nm, so the PAA pores do not close. In addition, the membrane thickness is ~3 μm, and the ratio of membrane thickness to pore diameter is more than 50. As a result, Fe atoms are not deposited at the pore bottom, as shown in the diagram presented in Fig. 3D. Moreover, the amount of Fe atoms deposited on the inner PAA pore walls decreases with increasing pore depth (the shading effect) [26,63,64].

Surface morphology analysis of the PAA membranes by SEM showed that their surface, when formed by two-stage anodization, turns out to be relief and non-planar. Thus, hexagonally ordered pores are located in the center of hemispherical cells with peaks and valleys (inset 2 in Fig. 3D). However, after ion-plasma treatment in an Ar atmosphere prior to Fe deposition, the surface relief is aligned and the peaks on the cell boundaries are smoothed out (inset 1 in Fig. 3B) [57,65].

3.2. Chemical composition of the Fe-PAA samples

Figs. 4–6 and Tables 2–4 show the results of the EDX analysis of the samples. Fig. 4 depicts multilayer EDX images for four types of samples: A, B, C are samples of types I, II, and III with a deposited Fe film of 95 ± 5 nm, and D is sample of type III with a Fe film thickness of 30 ± 5 nm.

As can be seen, in all multilayer EDX images (Fig. 4A–C), a mesh of Fe atoms is clearly visible, deposited along the edges of the oxide cells and partially inside the PAA pores. The mesh follows the shape of the PAA surface, with slightly smaller diameter pores due to the Fe atoms trapped inside the PAA pores. In multilayer EDX images, fragments of alumina "shine through" thinner areas of the Fe film. Obviously, the thickness of the Fe film is significantly less than 90 nm at these locations.

For sample type III with a 30 ± 5 nm thick Fe film, the situation is reversed (Fig. 4D). Fe atoms appear as red islands on a green background (surface of porous alumina). This is not a porous film with fragments of another material, but an island film in the form of discrete spots due to deposition on a relief surface.

Similar results were obtained on type I and II samples. Unfortunately, it was not possible to measure magnetic parameters by the VSM method on samples with an Fe film thickness of 30 nm. Therefore, further studies were carried out mainly on samples with an Fe film thickness of 100 nm.

Fig. 5 presents the elemental distribution maps of the Fe-PAA nanocomposite material of the type III sample.

Developed morphology of the PAA template surface can lead to a nonuniform deposition of Fe films as the peaks can become centers of iron crystallization. Nevertheless, the films are deposited over the entire surface between the pores. Figs. 3 and 4 show that all the components of the Fe-PAA nanocomposite material are well distributed over the entire surface of the samples. Fig. 6 depicts the EDX spectra for all types of the samples.

The results of the EDX analysis are presented in Table 2.

It can be seen that the ratio of the oxygen to aluminum atomic content in the initial PAA template is 1.48. It is close to the atomic ratio in stoichiometric Al_2O_3, 1.5. In the nanocomposite materials, this ratio is approximately 1.42, 1.48, and 1.45 (samples type I, II, and III, respectively).

Let us consider how the addition of Fe and its possible oxidation would affect this ratio. Let us assume that the material under investigation consists of 75 % Al_2O_3 and 15 % FeO. In this case, the oxygen-to-aluminum atomic ratio is $(3 \times 0.75 + 0.15)/(0.75 \times 2) = 1.6$. This means that iron oxidation would lead to an increase in the ratio value, which is not observed in our case.

This observation suggests that Fe is oxidized at the surface of the oxide and not during the deposition process. Formation of a 3–5 nm thick antiferromagnetic oxide films through oxidation of a small number of surface Fe atoms can slightly reduce the contribution to the magnetization of the entire sample, which is dominated by the main Fe atoms in the composition of the nanosized Fe mesh (under a thin oxide shell of FeO on the surface of the array) [18,67].

Previously, we assumed that Fe atoms were not deposited at the bottom of the PAA pores, but a certain number of atoms were deposited on the pore walls near the surface. To verify this assumption (the presence or absence of Fe in the pores), EDX analysis was carried out along lines passing through sections ~3 μm in length, including above the pores. Fig. 7 shows the EDX results of the Fe-PAA samples surface along

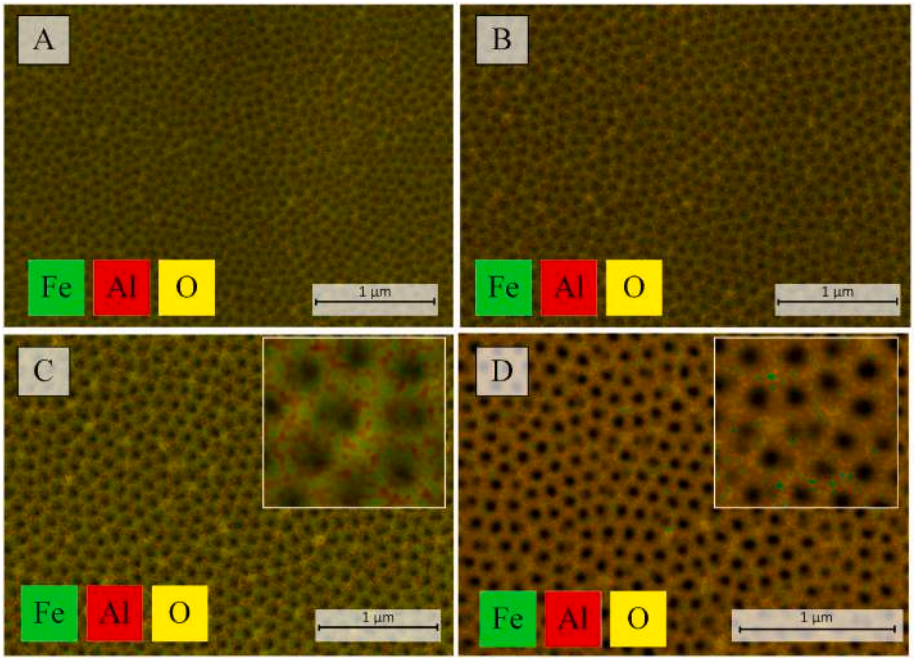

Fig. 4. Multilayer EDX images for samples of three types with a deposited Fe film of 95 ± 5 nm thickness: A, B, C – samples of types I, II, and III, respectively; D – sample of type III with a Fe film thickness of 30 ± 5 nm.

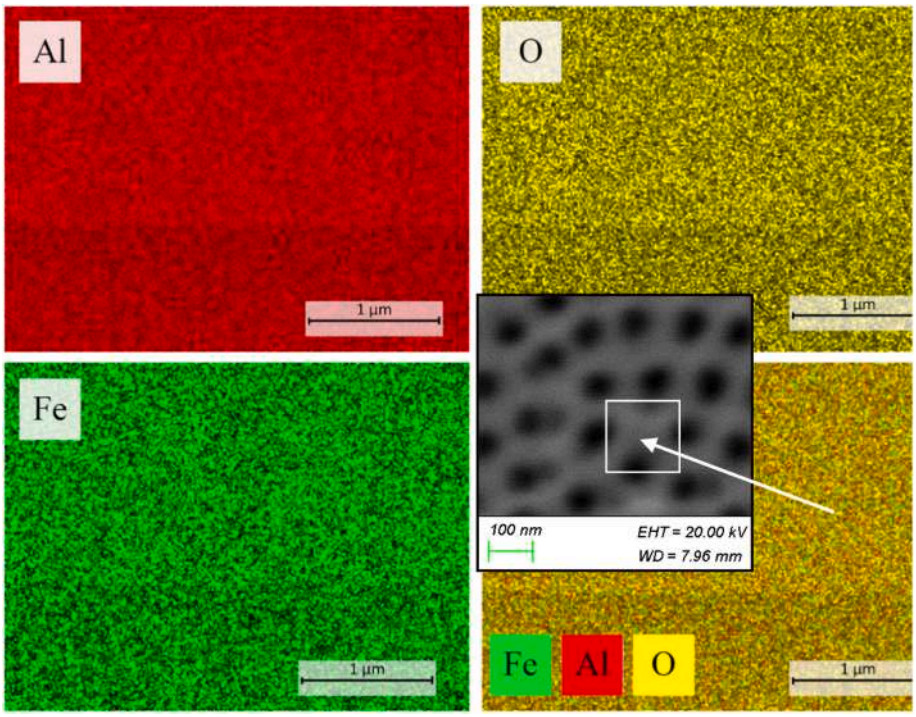

Fig. 5. Distribution maps of the main elements of the Fe-PAA nanocomposite material, showing how the elements are located in the analyzed area of the type III sample.

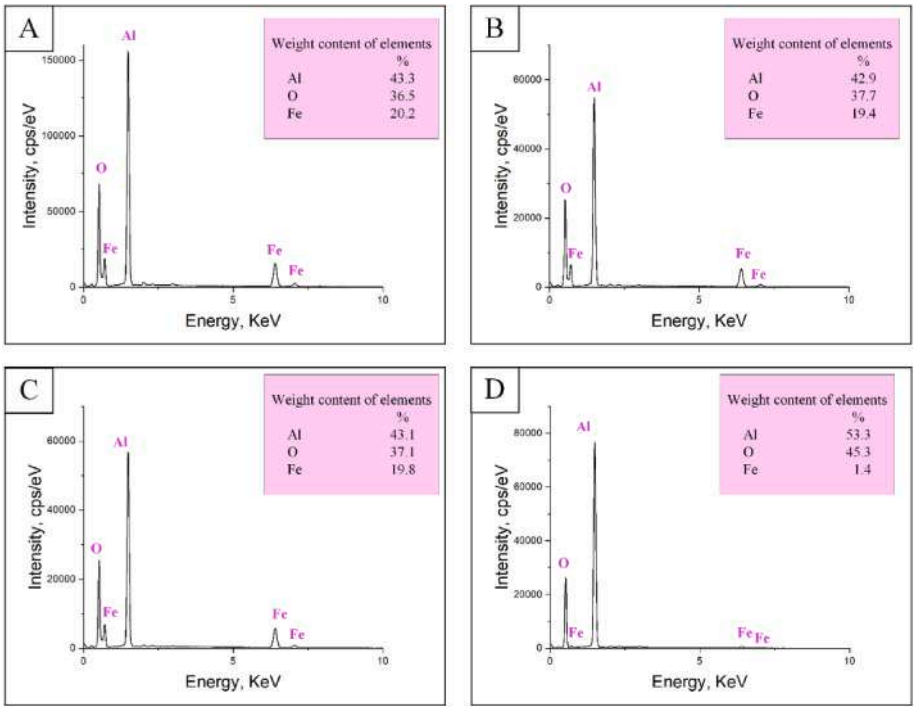

Fig. 6. Total EDX spectra of the samples: A, B, C – samples type I, II, and III, respectively, D – sample type III with Fe film of 30 ± 5 nm thickness.

the indicated lines (distribution of elements along the profile) in several sections.

The Fe signal is recorded across the entire analyzed surface and in the pores located on the line approximately equally in sample type I and sample type II (the analysis depth is < 1.5 μm). Only in sample type III with the largest pore size are there more expressive Fe signal variations at the pore locations (dashed lines in Fig. 7C), indicating that in this sample a greater number of Fe atoms are deposited on the pore walls.

Using SEM and EDX methods, it has been shown that the morphology of thin Fe films with a 90 nm thickness deposited on PAA templates with different morphological parameters and corresponding features of the surface relief completely repeats the relief of the porous templates used. Fe films are uniformly deposited on the region of PAA cells around the pores and partially into the pores, forming a cellular-porous hexagonally

Table 2
Elemental composition of the Fe-PAA nanocomposite for three types of samples compared with similar data for the initial alumina (prior to Fe deposition), presented in Ref. [66].

Element	PAA		Sample type I		Sample type II		Sample type III	
	Atom %	Weight %	Atom %	Weight %	Atom %	Weight %	Atom %	Weight %
Al	39.83	52.28	37.80	43.33	37.06	42.91	37.42	43.12
O	59.05 (1.48)[a]	45.97	53.70 (1.42)[a]	36.50	54.83 (1.48)[a]	37.65	54.29 (1.45)[a]	37.10
Fe	–	–	8.50	20.17	8.11	19.44	8.29	19.78
Sum	100.00	100.00	100.00	100.00	100.00	100.00	100.00	100.00

[a] ratio of the number of O atoms to Al atoms is shown in brackets.

Table 3
The main features of the XRD patterns of the Fe-PAA nanocomposites.

Sample type	Crystal orientation (HKL)	2 Theta, deg.	Intensity, %
I	Fe (110)	43.67 (43.91)[a]	5.91
	Fe (200)	65.50 (65.30)[a]	100
	Fe (220) + Al_2O_3	77.50 (75.25)[a]	59.09
II	Fe (110)	43.67 (43.91)[a]	6.25
	Fe (200)	65.50 (65.30)[a]	100
	Fe (220) + Al_2O_3	77.50 (75.25)[a]	54.17
III	Fe (110)	43.67 (43.91)[a]	4.76
	Fe (200)	65.50 (65.30)[a]	100
	Fe (220) + Al_2O_3	77.50 (75.25)[a]	31.50

[a] in column "2 Theta", the values from the JCPDS database are presented in parentheses.

ordered nanostructure.

3.3. Crystal structure of the Fe-PAA samples

Next, we will discuss the crystal structure of the samples. The XRD patterns of the Fe-PAA nanocomposites are shown in Fig. 8 and summarized in Table 3.

The narrow peak character of these XRD data indicates crystalline phase for all samples. The diffraction peaks were identified as the (110) and (200) reflections of typical α-Fe (JCPDS 06–0696) with a body-centered cubic lattice and ferromagnetic properties, and the result indicates that Fe films are polycrystalline. Similarly, the second and third narrow peaks at $2\theta = 65.30^\circ$ and 75.25° are labeled as (200) and (220) reflections, respectively, consistent with the nanocrystalline system. From the comparison of the intensities of the diffraction peaks, it is clear that the predominant direction of the growth orientation (texture) of the crystallites in the Fe film is the [200] direction. The XRD patterns also clearly indicate the preferred orientation change. Under similar deposition conditions, the preferred direction of crystallite growth for continuous Fe films is [110] [68].

The structure of the nanocomposite can be represented as a three-dimensional network in the cells of amorphous Al_2O_3, on the surface and inside of which there are metallic areas of Fe nanocrystals, i.e., a nanoporous film of Fe with pore sizes in the range of 50–80 nm on the PAA surface. Since the structural parameters of thin films (including Fe) are always related to the type and properties of the substrate on which the film is grown [69], the Fe (220) + Al_2O_3 peak is shifted.

Obviously, the main reason for the shift of the Fe (110) peak is the film thickness. In the work [68] it is shown how, with a decrease in the thickness of the deposited film, the structure and, accordingly, the XRD patterns of the Fe films change under different deposition conditions. According to these data, the grain size depends on the deposition conditions (primarily on temperature) and on the film thickness. For films with a thickness of ~100 nm deposited under conditions that are close to ours, it is approximately 6.5–7.0 nm. The presented data show that there is a shift of the Fe peak (110) with a change in the film thickness and explain the reasons for the preferred (200) orientation in Fe films with a thickness of ~100 nm in our work.

Thus, using the XRD method, it has been shown that the structural and phase characteristics of Fe films deposited on PAA template, despite the developed surface morphology, are similar to the structure of continuous Fe films and are determined by the deposition regime, substrate type, and Fe thickness.

3.4. Magnetic properties of the Fe-PAA samples

Further, the magnetic properties of the Fe-PAA nanocomposites have been studied, analyzed, and compared with those of bulk Fe films and literature data. External magnetic field H was oriented along the film surface (H//) and along its normal (H⊥) during the measurement of the magnetization curves M(H). The measurement temperatures were 4.2 and 300 K. The diamagnetic contribution of the PAA substrate was subtracted from the obtained magnetization values. The experimental M (H) plots for all sample types are shown in Fig. 9.

The detailed information on magnetic parameters of the Fe-PAA nanocomposites is shown in Table 4.

From the presented results, it is clear that the magnetic parameters of the studied Fe-PAA nanocomposites are significantly higher than those of bulk α-Fe and of Fe films of comparable thickness (95 ± 5 nm). The results of magnetic measurements also show that nanoporous Fe films have perpendicular anisotropy with pronounced magnetic anisotropy along the normal to their surface. All types of Fe films are characterized by perpendicular magnetic anisotropy with an increase in the coercive force $H_C\perp$ by about 1.6 times when measured in perpendicular geometry, compared with the curves obtained in the Fe film plane ($H_C\perp \approx 300$ Oe и $H_C// \approx 180$ Oe for the Fe films in Sample type I and Sample type III) and 2.4 times for sample type II films. A peculiar feature of the porous

Table 4
Comparison of magnetic parameters of the Fe-PAA nanocomposites for different sample types.

T, K	U, V	H_c, ⊥ Oe	H_c,//Oe	M_r, ⊥ emu/g	Mr,//emu/g	M_s, ⊥ emu/g	Ms,//emu/g	M_r/M_s ⊥	Mr/Ms //
300	40 I	292	182	0.068	0.322	0.502	0.669	0.14	0.40
	50 II	328	135	0.209	0.268	0.699	0.520	0.30	0.45
	60 III	282	179	0.072	0.220	0.400	0.413	0.18	0.55
	Fe thin films [68,70]	–	30–80[a]	–	–	–	–	–	–
4.2	40 I	512	372	0.087	0.575	0.591	0.800	0.15	0.72
	50 II	602	205	0.215	0.425	0.807	0.599	0.29	0.71
	60 III	441	344	0.091	0.302	0.499	0.511	0.18	0.60

[a] for Fe films with 95 ± 5 nm thickness under the same deposition conditions as in [68,70].

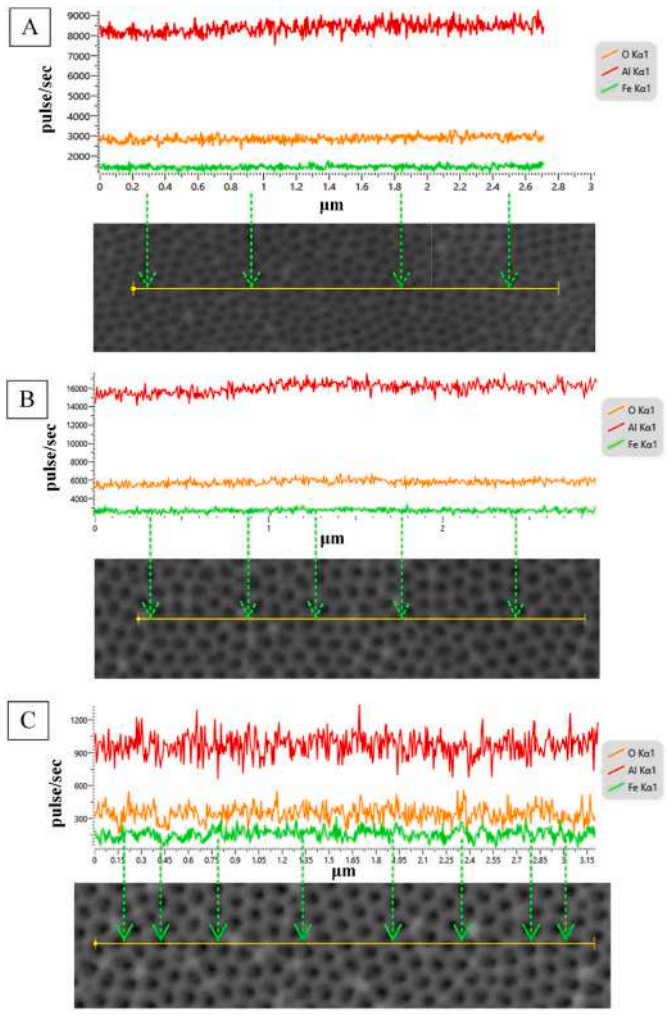

Fig. 7. EDX analysis results of the Fe-PAA samples surface along the indicated lines: A – sample of type I, B – sample of type II, C – sample of type III.

films is the reduction in the quadratic nature of the M(H⊥) dependencies to ~0.14–0.18 (for two temperatures there are almost identical values), which may be due to a violation of the co-direction of magnetic moments in material deposited on different areas of PAA substrates. Continuous Fe films of comparable thickness exhibit isotropic in-plane (horizontal property anisotropy) magnetic hysteresis with relatively low coercivity and high squareness loops characteristic of soft Fe films [68,70].

An almost twofold increase in H_C is observed for porous Fe films for all sample types, which is explained by the pinning of magnetic moments deviating from the normal to the films at artificially created defects (pores and cell boundaries) [27,50]. That is, the main role in the formation of a complex of magnetic parameters of nanoporous Fe films on the PAA template surface is played by the volumetric structure of the nanocomposite and the morphology of the PAA surface, which are determined by the synthesis method. Conventional magnetic films have anisotropy of the "easy plane" type (horizontal anisotropy of properties), i.e., it is advantageous for the magnetic moment to be oriented along the plane of the film. To magnetize a film perpendicular to its surface, it is necessary to apply an external field that exceeds the demagnetization field and is greater than 10000 Oe for films of ferromagnetic transition group metals (Fe, Co, Ni) [71]. In order to qualitatively change the situation and achieve conditions where it is advantageous for the magnetic moment to be oriented normal to the film surface, there are two methods. The first approach is to change the shape of the film by nanostructuring. The second one is to create artificial anisotropy of the "easy axis" type at the boundary of ferromagnetic films and noble metals (usually Pt, Pd). The presence of an interface will lead to the appearance of surface anisotropy due to spin-orbit interaction. It has been shown theoretically and experimentally that for some pairs of materials the surface anisotropy is an "easy axis" anisotropy, and its value exceeds the value of the demagnetizing field [72,73]. In this work, we used the first method – nanostructuring. Fe films with the thickness of 95 ± 5 nm additionally deposited on silicon substrates in a single vacuum cycle had similar coercive force values ($H_C\perp \approx 55$ Oe and $H_C// \approx 35$ Oe) and horizontal anisotropy.

3.5. Thermodynamic studies of the Fe-PAA samples

To study the thermodynamic characteristics, a complex thermal analysis system was used – a method that records the temperature difference between the sample and the standard (DTA), as well as the change in sample mass depending on temperature and time (TGA). As a result, TGA curves were obtained – the dependence of the change in sample mass on temperature and time. To interpret the results of TGA analysis, TGA curves were processed. In particular, the derivative of the TGA signal (the rate of mass change), represented by the DTA curve, made it possible to accurately determine the time and temperature at which the weight change occurs most rapidly.

In our previously published article [64], it was shown that PAA membranes made from Al foil (99.995 %) by two-stage anodization in a 4 % aqueous solution of oxalic acid are sufficiently chemically and thermally stable in the temperature range from room temperature to 850 °C. Therefore, the studies were carried out in the temperature range from 25 °C to 900 °C [74]. Fig. 10 shows the results of a TDA study of the Fe/PAA nanocomposite in air.

It is known that at the Shadron's temperature (575 °C) a film of $FeO_{0.947}$ is formed on the surface of bulk Fe, on top of which there is an Fe_3O_4 oxide [75]. That is, at a temperature above 575 °C a two-layer film of Fe oxide exists stably. It has been shown [76] that with decreasing particle size their surface energy increases and as a consequence the Gibbs potential energy decreases, which leads to an increase in the reactivity of the particles. Therefore, it is possible that the thinner the Fe film, the lower the minimum temperature of oxide formation. In our nanocomposite samples, the oxidation process begins at 520 °C in air. That is, at a temperature of 520 °C, a two-layer Fe oxide film stably exists on the surface of the Fe film. With a further increase in temperature, the remaining Fe film gradually oxidizes through at a temperature of 655 °C. However, as can be seen from the presented diagrams in Fig. 1, annealing at a temperature of 500 °C and higher (up to 600 °C) does not lead to a phase transition (melting of the Fe film). Recrystallization and, simultaneously, through oxidation of the Fe film occur.

Theoretically, the temperature of the onset of recrystallization is a certain fraction of the melting temperature of the metal: $T_{recr} = a \times T_{melt}$ [77]. The value of the coefficient a depends on the purity of the metal and the degree of plastic deformation, in this case caused by the difference in the thermoelastic characteristics of the components of the nanocomposite material (thermal coefficient of linear expansion for Fe and PAA). For metals of technical purity, a = 0.3–0.4 and decreases with increasing degree of deformation. That is, for bulk Fe the temperature of the beginning of recrystallization can be in the range from 462 to 615 °C. It can be assumed that in this range from 462 to 500 °C recrystallization occurs in the Fe film, and in the range up to 615 (655) °C through oxidation occurs. However, as can be seen from the presented diagrams, annealing at a temperature of 500 °C and higher (up to 655 °C) does not lead to a phase transition (melting of the Fe film).

4. Conclusion

A technological method has been developed to fabricate nanoporous Fe films on the surface of PAA templates with different morphological parameters. Experimental samples of three types of Fe-PAA

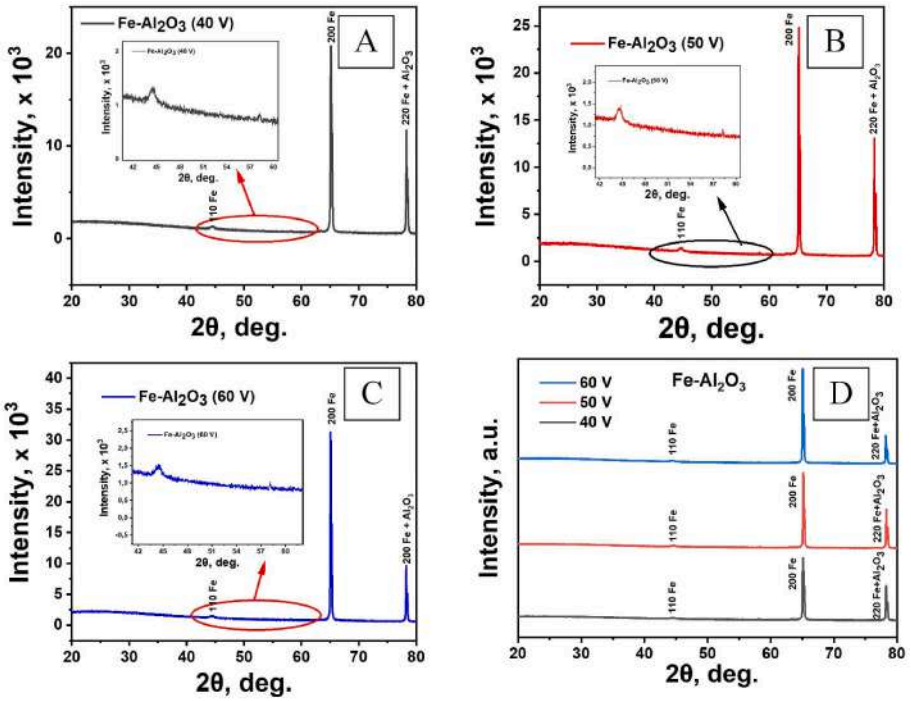

Fig. 8. XRD patterns of the Fe-PAA nanocomposites: A, B, C – samples of types I, II, and III, respectively; D – comparison of the XRD patterns for all samples.

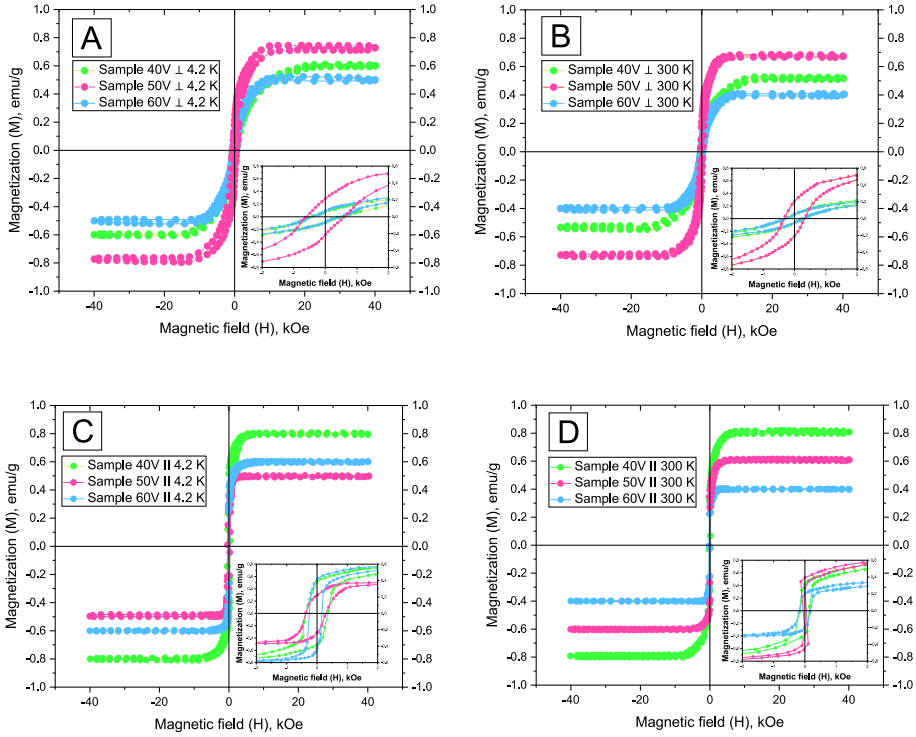

Fig. 9. M(H) magnetization curves of the Fe-PAA nanocomposite samples obtained along their normal (H⊥) and in the surface plane (H//) at 300 and 4.2 K for different sample types.

nanocomposites with different pore diameters were prepared. The method and regimes developed are compatible with the silicon production technology of micro- and nanoelectronic devices.

Using SEM and EDX methods, it has been shown that the morphology of thin Fe films deposited on PAA templates with different morphological parameters and corresponding surface topography features completely replicates that of the porous template used. The films are uniformly deposited on the region of the PAA cells around the pores and partially into the pores, forming a cellular-porous hexagonally ordered nanostructure.

It has been shown by XRD technique that the structural and phase characteristics of the Fe-PAA nanocomposite, in spite of the developed surface morphology, are similar to the structure of solid Fe films and are determined by the deposition regime, substrate type, and Fe thickness.

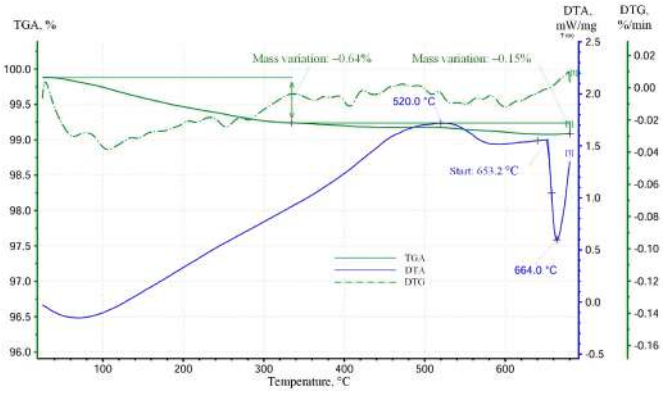

Fig. 10. Results of the TDA analysis of Fe-PAA nanocomposite in air atmosphere.

The XRD patterns also clearly indicate preferred orientation change. The predominant direction of crystallite growth orientation in a porous Fe film is the [200] direction, whereas for solid Fe films, the [110] direction is predominant under similar deposition conditions.

The magnetic parameters of the Fe-PAA nanocomposites were found to be significantly higher than those of bulk α-Fe and Fe films of comparable thickness (95 ± 5 nm). The results of magnetic measurements showed that nanoporous Fe films have perpendicular anisotropy of properties with pronounced magnetic anisotropy along the normal to their surface. The controlled magnetic properties of the obtained Fe films allow a wide range of practical applications: for the fabrication of magnetically sensitive transistors, chemical and biochemical sensors, magnonic crystals, and as a material for nanoelectrodes for studying electrochemical processes in the nanometer range.

Thermodynamic studies have shown the high thermal stability of the obtained Fe-PAA nanocomposite material to a temperature up to 600 °C. In addition, it has been determined the temperature of through oxidation of the Fe film. Currently, the staged thermal oxidation of the obtained Fe-PAA nanocomposites is being studied to obtain nanostructured porous iron oxide films on the PAA template Fe_3O_4-PAA.

CRediT authorship contribution statement

D.I. Tishkevich: Writing – review & editing, Writing – original draft, Supervision, Methodology, Investigation, Funding acquisition, Conceptualization. **A.I. Vorobjova:** Writing – review & editing, Writing – original draft, Visualization, Investigation, Conceptualization. **E.A. Outkina:** Investigation. **S.M. Zavadskii:** Investigation. **I.U. Razanau:** Validation. **T.I. Zubar:** Investigation, Formal analysis. **A.A. Bondaruk:** Writing – original draft, Visualization, Software. **A.A. Rotkovich:** Writing – review & editing, Visualization, Data curation. **M.I. Sayyed:** Methodology, Investigation. **M.V. Silibin:** Writing – original draft, Project administration, Investigation. **A. Yu Gerasimenko:** Writing – review & editing, Funding acquisition. **O.A. Sycheva:** Investigation, Writing – review & editing. **S.V. Trukhanov:** Validation, Resources. **A. V. Trukhanov:** Writing – original draft, Supervision, Project administration, Investigation, Funding acquisition.

Funding

The work was carried out as part of a major scientific project with financial support from the Russian Federation represented by the Ministry of Science and Higher Education of the Russian Federation under agreement No. 075-15-2024-555 dated April 25, 2024.

Declaration of competing interest

The authors declare that they have no known competing financial interests or personal relationships that could have appeared to influence the work reported in this paper.

Acknowledgment

Authors are grateful for financial support from Belarusian Republican Foundation for Fundamental Research project (BRFBR project N°. Ф23РНФМ-059).

Data availability

Data will be made available on request.

References

[1] G.I. Frolov, O.I. Bachina, M.M. Zavyalova, S.I. Ravochkin, Magnetic properties of 3d-metal nanoparticles, J. Tech. Phys. 78 (8) (2008) 101106, https://doi.org/10.1134/S1063784208080136.
[2] R. Glaser, Biophysics: an Introduction, Springer Verlag, 1999, p. 362, https://doi.org/10.1007/978-3-642-25212-9.
[3] S. Michea, J.L. Palma, R. Lavın, J. Briones, J. Escrig, J.C. Denardin, R.L. Rodrıguez-Suarez, Tailoring the magnetic properties of cobalt antidot arrays by varying the pore size and degree of disorder, J. Phys. D 47 (2014) 335001, https://doi.org/10.1088/0022-3727/47/33/33500.
[4] A. Manzin, G. Barrera, F. Celegato, M. Cöısson, P. Tiberto, Influence of lattice defects on the ferromagnetic resonance behaviour of 2D magnonic crystals, Sci. Rep. 6 (2016) 22004, https://doi.org/10.1038/srep22004.
[5] S. Tacchi, P. Gruszecki, M. Madami, G. Carlotti, J.W. Kłos, M. Krawczyk, A. Adeyeye, G. Gubbiotti, Universal dependence of the spin wave band structure on the geometrical characteristics of two-dimensional magnonic crystals, Sci. Rep. 5 (2015) 10367, https://doi.org/10.1038/srep10367.
[6] K.L. Metlov, Topological memory with multiply-connected planar magnetic nanoelements, JETP Lett. 118 (2023) 105–111, https://doi.org/10.1134/S0021364023601823.
[7] E.B. Magadeev, R.M. Vakhitov, Structure of magnetic inhomogeneities in films with topological features, JETP Lett. 115 (2022) 114–118, https://doi.org/10.1134/S0021364022020060.
[8] F. Spizzo, P. Sgarbossa, E. Sieni, A. Semenzato, F. Dughiero, M. Forzan, R. Bertani, L. Del Bianco, Synthesis of ferrofluids made of iron oxide nanoflowers: interplay between carrier fluid and magnetic properties, Nanomaterials (Basel) 7 (11) (2017) 373, https://doi.org/10.3390/nano7110373.
[9] Y.-W. Jun, J.-W. Seo, J. Cheon, Nanoscaling laws of magnetic nanoparticles and their applicabilities in biomedical sciences, Acc. Chem. Res. 41 (2) (2008) 179, https://doi.org/10.1021/cr900137k.
[10] N. Singh, G.J.S. Jenkins, R. Asadi, S.H. Doak, Potential toxicity of superparamagnetic iron oxide nanoparticles (SPION), Nano Rev. 1 (1) (2010) 5458, https://doi.org/10.3402/nano.v1i0.5358.
[11] E.N. Maksimova, T.P. Denisova, E.V. Simonova, A.P. Safronov, V.I. Pedranova, I. N. Egorova, O.M. Samatov, G.V. Kurlyandskaya, Effect of magnetic ferric oxide (γ-Fe_2O_3) nanoparticles on the growth of algal and yeast culture, inorganic materials, Appl. Res. 11 (4) (2020) 772, https://doi.org/10.1134/S2075113320040255.
[12] S.A.M. Khawja Ansari, E. Ficiara, F.A. Ruffinatti, I. Stura, M. Argenziano, O. Abollino, R. Cavalli, C. Guiot, F. D'Agata, Magnetic iron oxide nanoparticles: synthesis, characterization and functionalization for biomedical applications in the central nervous system, Mater 12 (3) (2019) 465, https://doi.org/10.3390/ma12030465.
[13] M.R. Zamani Kouhpanji, B.J.H. Stadler, A guideline for effectively synthesizing and characterizing magnetic nanoparticles for advancing nanobiotechnology: a review, Sensors (Peterb., NH) 20 (9) (2020) 2554, https://doi.org/10.3390/ma12030465.
[14] C. Kim, T. Loedding, S. Jang, H. Zeng, Z. Li, Y. Sui, D.J. Sellmyer, FePt nanodot arrays with perpendicular easy axis, large coercivity, and extremely high density, Appl. Phys. Lett. 91 (2007) 172508, https://doi.org/10.1063/1.2802038.
[15] T. Seki, T. Shima, K. Yakushiji, K. Takanashi, G.Q. Li, S. Ishio, Dot size dependence of magnetic properties in microfabricated FePt (001) and FePt (110) dot arrays, J. Appl. Phys. 100 (2006) 043915, https://doi.org/10.1063/1.2335391.
[16] C.A. Ross, M. Hwang, M. Shima, J.Y. Cheng, M. Farhoud, T.A. Savas, H.I. Smith, W. Schwarzacher, F.M. Ross, M. Redjdal, F.B. Humphrey, Micromagnetic behavior of electrodeposited cylinder arrays, Phys. Rev. B 65 (2002) 144417, https://doi.org/10.1103/PhysRevB.65.144417.
[17] H. Wang, Y.C. Wu, L. Zhang, X. Hu, Fabrication and magnetic properties of FePt multilayered nanowires, Appl. Phys. Lett. 89 (2006) 232508, https://doi.org/10.1063/1.2402888.
[18] K.-T. Huang, P.-C. Kuo, Y.-D. Yao, Formation of Pt nanorods on nanoporous anodic aluminum oxides by controlled nucleation sites, Thin Solid Films 518 (2010) 5300–5303, https://doi.org/10.1016/j.tsf.2008.11.069.
[19] L.J. Heyderman, F. Nolting, D. Backes, S. Czekaj, L. LopezDiaz, M. Klaui, U. Rüdiger, C.A.F. Vaz, J.A.C. Bland, R.J. Matelon, U.G. Volkmann, P. Fischer, Magnetization reversal in cobalt antidot arrays, Phys. Rev. B 73 (2006) 214429, https://doi.org/10.1103/PhysRevB.73.214429.
[20] M.M. Miller, G.A. Prinz, S.-F. Cheng, S. Bounnak, Detection of a micron-sized magnetic sphere using a ring-shaped anisotropic magnetoresistance-based sensor: a

model for a magnetoresistance-based biosensor, Appl. Phys. Lett. 81 (2002) 2211, https://doi.org/10.1063/1.1507832.
[21] G. Neri, A. Bonavita, S. Galvagno, N. Donato, A. Caddemi, Electrical modeling of Fe_2O_3 humidity sensors doped with Li^+, Zn^{2+} and Au^{3+} ions, Sens. Actuators, A 111–112 (2005) 71–77, https://doi.org/10.1016/j.snb.2005.06.061.
[22] R. Li, L. Cao, C. Liang, S. Sun, H. Liu, P. Yan, Development and modeling of an ultrasensitive label-free electrochemical immunosensor for okadaic acid based on polythionine-modified three-dimensional gold nanoelectrode ensembles, Ionics (Kiel) 26 (2020) 4661–4670, https://doi.org/10.1007/s11581-020-03599-1.
[23] D.S. Kim, E.S. Kang, S. Baek, S.S. Choo, Y.H. Chung, D. Lee, J. Min, T.H. Kim, Electrochemical detection of dopamine using periodic cylindrical gold nanoelectrode arrays, Sci. Rep. 8 (2018) 14049, https://doi.org/10.1038/s41598-018-32477-0.
[24] A.O. Adeyeye, N. Singh, Large area patterned magnetic nanostructures, J. Phys. 41 (2008) 153001, https://doi.org/10.1088/0022-3727/41/15/153001.
[25] S. Pal, J.W. Klos, K. Das, O. Hellwig, P. Gruszecki, M. Krawczyk, A. Barman, Optically induced spin wave dynamics in [Co/Pd]8 antidot lattices with perpendicular magnetic anisotropy, Appl. Phys. Lett. 105 (2014) 162408, https://doi.org/10.1063/1.4898774.
[26] M.T. Rahman, N.N. Shams, C.H. Lai, J. Fidler, D. Suess, Co/Pt perpendicular antidot arrays with engineered feature size and magnetic properties fabricated on anodic aluminum oxide templates, Phys. Rev. B 81 (2010) 014418, https://doi.org/10.1103/PhysRevB.81.014418.
[27] A. Maximenko, J. Fedotova, M. Marszalek, A. Zarzycki, Y. Zabila, Magnetic characteristics of CoPd and FePd antidot arrays on nanoperforated Al2O3 templates, J. Magn. Magn Mater. 400 (2016) 200, https://doi.org/10.1016/j.jmmm.2015.08.057.
[28] M.E. Molares, V. Buschmann, D. Dobrev, R. Neumann, R. Scholz, I.U. Schuchert, J. Vetter, Single-crystalline copper nanowires produced by electrochemical deposition in polymeric Ion track membranes, Adv. Mater. 13 (2001) 62–65, https://doi.org/10.1002/1521-4095(200101)13:1<62::AID-ADMA62>3.0.CO;2-7.
[29] S. Mátéfi-Tempfli, M. Mátéfi-Tempfli, A. Vlad, Nanowires and nanostructures fabrication using template methods: a step forward to real devices combining electrochemical synthesis with lithographic techniques, J. Mater. Sci. Mater. Electron. 20 (1) (2009) S249–S254, https://doi.org/10.1007/s10854-008-9568-6.
[30] C.T. Sousa, D.C. Leitao, M.P. Proenca, J. Ventura, A.M. Pereira, J.P. Araujo, Nanoporous alumina as templates for multifunctional applications, Appl. Phys. Rev. 1 (2014) 031102, https://doi.org/10.1063/1.4893546.
[31] W. Lee, S.-J. Park, Porous anodic aluminum oxide: anodization and templated synthesis of functional nanostructures, Chem. Rev. 114 (2014) 7487–7556, https://doi.org/10.1021/cr500002z.
[32] D. Brüggemann, Nanoporous aluminium oxide membranes as cell interfaces, J. Nanomater. (2013) 1–18, https://doi.org/10.1155/2013/460870.
[33] C.S. Law, G. Sylvia, M. Nemati, Engineering of surface chemistry for enhanced sensitivity in nanoporous interferometric sensing platforms, App. Mat. Inter. 9 (10) (2017) 8929–8940, https://doi.org/10.1021/acsami.7b01116.
[34] S. Jelveh, D. Chithrani, Gold nanostructures as a platform for combinational therapy in future cancer therapeutics, Cancers 3 (2011) 1081–1110, https://doi.org/10.3390/cancers3011081.
[35] A.A. Vasiliev, R.G. Pavelko, S.Y. Gogish-Klushin, Alumina MEMS platform for impulse semiconductor and IR optic gas sensors, Sensor. Actuator. B Chem. 132 (2008) 216–223, https://doi.org/10.1016/j.snb.2008.01.043.
[36] H. Feng, J.W. Elam, J.A. Libera, Catalytic nanoliths, Chem. Eng. Sci. 64 (2009) 560–567, https://doi.org/10.1016/j.ces.2008.09.027.
[37] F.A. Blyakhman, E.B. Makarova, F.A. Fadeyev, D.V. Lugovets, A.P. Safronov, P. A. Shabadrov, T.F. Shklyar, G.Yu Melnikov, I. Orue, G.V. Kurlyandskaya, The contribution of magnetic nanoparticles to ferrogel biophysical properties, Nanomaterials (Basel) 9 (2) (2019) 232, https://doi.org/10.3390/nano9020232.
[38] N.A. Buznikov, A.P. Safronov, I. Orue, E.V. Golubeva, V.N. Lepalovskij, A. V. Svalov, A.A. Chlenova, G.V. Kurlyandskaya, Modelling of magnetoimpedance response of thin film sensitive element in the presence of ferrogel: next step toward development of biosensor for in-tissue embedded magnetic nanoparticles detection, Biosens. Bioelectron. 117 (2018) 366, https://doi.org/10.1016/j.bios.2018.06.032.
[39] S. Leulmi, X. Chauchet, M. Morcrette, G. Ortiz, H. Joisten, P. Sabon, T. Livache, Y. Hou, M. Carrière, S. Lequiena, B. Dieny, Triggering the apoptosis of targeted human renal cancer cells by the vibration of anisotropic magnetic particles attached to the cell membrane, Nanoscale 7 (38) (2015) 15904, https://doi.org/10.1039/C5NR03518J.
[40] A.I. Vorobjova, D.I. Tishkevich, E.A. Outkina, Y. Yao, I.U. Razanau, T.I. Zubar, A. A. Rotkovich, A.A. Bondaruk, M.I. Sayyed, S.V. Trukhanov, I.V. Kubasov, V. M. Fedosyuk, A.V. Trukhanov, Fabrication of composite nanostructures for impedance biosensors using nodic aluminum oxide templates and carbon nanotubes, Ceram. Int. 50 (2024) 45703–45712, https://doi.org/10.1016/j.ceramint.2024.08.411.
[41] S.V. Denisyuk, N.I. Mukhurov, O.N. Kunovich, Two-zone gas sensors on Al2O3 substrates with thin-film detectors of iron oxide elements, Nano- and Microsystems Engineering 11 (2018) 676–688.
[42] G.V. Kurlyandskaya, E. Fernandez, A.P. Safronov, A.V. Svalov, I.V. Beketov, A. Burgoa Beitia, A. García-Arribas, F.A. Blyakhman, Giant magnetoimpedance biosensor for ferrogel detection: model system to evaluate properties of natural tissue, Appl. Phys. Lett. 106 (19) (2015) 193702, https://doi.org/10.1063/1.4921224.
[43] G.V. Kurlyandskaya, D.S. Portnov, I.V. Beketov, A. Larrãnaga, A.P. Safronov, I. Orue, A.I. Medvedev, A.A. Chlenova, M.B. Sanchez-Ilarduya, A. Martinez-Amesti, A.V. Svalov, Nanostructured materials for magnetic biosensing, Biochim. Biophys. Acta 1861 (6) (2017) 1494, https://doi.org/10.1016/j.bbagen.2016.12.003.
[44] Q. Wei, Y. Fu, G. Zhang, D. Yang, G. Meng, S. Sun, Rational design of novel nanostructured arrays based on porous AAO templates for electrochemical energy storage and conversion, Nano Energy 55 (2018) 234–259, https://doi.org/10.1016/j.nanoen.2018.10.070.
[45] G. Eddy, J. Poinern, Electrochemical synthesis, characterisation, and preliminary biological evaluation of an anodic aluminium oxide membrane with a pore size of 100 nanometres for a potential cell culture substrate, Am. J. Biomed. Res. 3 (6) (2013) 119–131, https://doi.org/10.5923/j.ajbe.20130306.01.
[46] P. Jai, E. Gerrard, A. Nurshahidah, F. Derek, Progress in nano-engineered anodic aluminum oxide membrane developmens, Mater 4 (3) (2011) 487–526, https://doi.org/10.3390/ma4030487.
[47] A.I. Vorobyova, E.A. Outkina, O.M. Komar, Study of metal pillar nanostructure formation with thin porous alumina template, Thin Solid Films 548 (2013) 109–117, https://doi.org/10.1016/j.tsf.2013.09.016.
[48] D.I. Tishkevich, A. Vorobjova, D. Shimanovich, Magnetic properties of the densely packed ultra-long Ni nanowires encapsulated in alumina membrane, Nanomat 11 (2021) 1775, https://doi.org/10.3390/nano11071775.
[49] A.I. Vorobjova, D.I. Tishkevich, E.A. Outkina, A study of Ta_2O_5 nanopillars with Ni tips prepared by porous anodic alumina through-mask anodization, Nanomat 12 (2022) 1344, https://doi.org/10.3390/nano12081344.
[50] A.A. Maximenko, J.V. Kasiuk, J.A. Fedotova, M. Marszałek, Y. Zabila, J. Chojenka, Magnetic properties of Co/Pd multilayered films on porous Al_2O_3 templates with developed cell substructure, Phys. Solid State 59 (9) (2017) 1762–1770, https://doi.org/10.1134/S1063783417090189.
[51] J. Xu, L. Chen, A. Mathewson, K.M. Razeeb, Ultra-long metal nanowire arrays on solid substrate with strong bonding, Nanoscale Res. Lett. 6 (525) (2011) 1–7, https://doi.org/10.1186/1556-276X-6-525.
[52] H.U. Osmanbeyoglu, T.B. Hur, H.K. Kim, Thin alumina nanoporous membranes for similar size biomolecule separation, J. Membrane Sci. 343 (2009) 1–6, https://doi.org/10.1016/j.memsci.2009.07.027.
[53] T. Yanagishita, H. Masuda, High-throughput fabrication process for highly ordered through-hole porous alumina membranes using two-layer anodization, Electrochim. Acta 184 (2015) 80–85, https://doi.org/10.1016/j.electacta.2015.10.019.
[54] Q. Hao, H. Huang, X. Fan, X. Hou, Y. Yin, W. Li, L. Si, H. Nan, H. Wang, Y. Mei, T. Qiu, P.K. Chu, Facile design of ultra-thin anodic aluminum oxide membranes for the fabrication of plasmonic nanoarray, Nanotech 28 (2017) 105301, https://doi.org/10.1088/1361-6528/aa596d.
[55] N. Verma, K.C. Singh, J. Jindal, Fabrication of nanomaterials on porous anodic alumina template using various techniques, Indian J. Adv. Chem. Sci. 3 (3) (2015) 235–246, https://doi.org/10.1023/A:1024479827507.
[56] A.I. Vorobjova, D.L. Shimanovich, K.I. Yanushkevich, Properties of Ni and Ni-Fe nanowires electrochemically deposited into a porous alumina template, Beilstein J. Nanotechnol. 7 (2016) 1709–1717, https://doi.org/10.3762/bjnano.7.163.
[57] A.I. Vorobjova, D.L. Shimanovich, E.A. Outkina, Highly ordered through-holes porous alumina membranes for nanowires fabrication, Appl. Phys. Mater. Sci. Process 1 (2018) 124–132, https://doi.org/10.1007/s00339-017-1401-8.
[58] S.V. Trukhanov, A.V. Trukhanov, L.V. Panina, V.G. Kostishyn, V.A. Turchenko, E. L. Trukhanova, A.V. Trukhanov, T.I. Zubar, V.M. Ivanov, D.I. Tishkevich, D. A. Vinnik, S.A. Gudkova, D.S. Klygach, M.G. Vakhitov, P. Thakur, A. Thakur, Y. Yang, Temperature evolution of the structure parameters and exchange interactions in $BaFe_{12-x}In_xO_{19}$, J. Magn. Magn Mater. 466 (2018) 393–405, https://doi.org/10.1016/j.jmmm.2018.07.041.
[59] J.P. O'Sullivan, G.C. Wood, The morphology and mechanism of formation of porous anodic films on aluminium, Proc. Roy. Soc. Lond. 317 (1970) 511–543, https://doi.org/10.1098/rspa.1970.0129.
[60] K. Nielsch, J. Choi, K. Schwirn, Self-ordering regimes of porous alumina: the 10 porosity rule, Nano Lett. 2 (2002) 677–680, https://doi.org/10.1021/nl025537k.
[61] G.D. Sulka, Temperature influence on well-ordered nanopore structures grown by anodization of aluminium in sulphuric acid, Electrochim. Acta 52 (2007) 1880–1888, https://doi.org/10.1016/j.electacta.2006.07.053.
[62] Y. Lei, W. Cai, G. Wilde, Highly ordered nanostructures with tunable size, shape and properties: a new way to surface nano-patterning using ultra-thin alumina masks, Prog. Mater. Sci. 52 (2007) 465–539, https://doi.org/10.1016/j.pmatsci.2006.07.002.
[63] Y. Lei, W.K. Chim, Shape and size control of regularly arrayed nanodots fabricated using ultrathin alumina masks, Chem. Mater. 17 (2005) 580, https://doi.org/10.1021/cm048609c.
[64] T. Karabacak, T.M. Lu, Enhanced step coverage by oblique angle physical vapor deposition, J. Appl. Phys. 97 (2005) 124504, https://doi.org/10.1063/1.1937476.
[65] D.L. Shimanovich, A.I. Vorobjova, D.I. Tishkevich, Preparation and morphology-dependent wettability of porous alumina membranes, Beilstein J. Nanotechnol. 9 (2018) 1423–1426, https://doi.org/10.3762/bjnano.9.135.
[66] A.I. Vorobjova, D.L. Shimanovich, O.A. Sycheva, T.I. Ezovitova, A.V. Trukhanov, D.I. Tishkevich, Research of thermodynamic characteristics of the composite magnetic medium on the basis of anodic alumina, Russ. Microelectron. 48 (2) (2019) 134–146, https://doi.org/10.1134/S1063739719020100.
[67] S.P. Li, W.S. Lew, Y.B. Xu, A. Hirohata, A. Samad, F. Baker, J.A.C. Bland, Magnetic nanoscale dots on colloid crystal surfaces, Appl. Phys. Lett. 76 (2000) 748, https://doi.org/10.1063/1.125882.
[68] Y.K. Kim, M. Oliveria, Magnetic properties of sputtered Fe thin films: processing and thickness dependence, J. Appl. Phys. 74 (2) (1993) 15, https://doi.org/10.1063/1.354926.

[69] A.L. Ravensburg, G.K. Pálsson, M. Pohlit, Influence of misfit strain on the physical properties of Fe thin films, Thin Solid Films 761 (2022) 139494, https://doi.org/10.1016/j.tsf.2022.139494.
[70] M. Prutton, Thin ferromagnetic films, Nature 206 (1964) 436–437, https://doi.org/10.1038/206436b0.
[71] J.L. Simonds, Magnetoelectronics today and tomorrow, Phys. Today 48 (4) (1995) 26–32, https://doi.org/10.1063/1.881482.
[72] P.F. Carcia, A.D. Meinhaldt, A. Suna, Perpendicular magnetic anisotropy in Pd/Co thin film layered structures, Appl. Phys. Lett. 47 (2) (1985) 178–180, https://doi.org/10.1063/1.96254.
[73] S.A. Gusev, YuN. Nozdrin, D.B. Rozenstein, A.A. Fraerman, M.G. Teitelman, M. G. Shirokov, Fluctuation induced reorientation transition in Co/Pd multilayered films, Physica B 198 (1994) 177–180, https://doi.org/10.1016/0921-4526(94)90155-4.
[74] A.I. Vorob'eva, D.L. Shimanovich, O.A. Sycheva, Studying the thermodynamic characteristics of anodic alumina 2018, Mikroelektronika 47 (1) (2018) 40–49, https://doi.org/10.1134/S1063739718010080.
[75] F.A. Brockhaus, Brockhaus and Ephron Encyclopaedic Dictionary, M.: Ripol Classic, 2013, p. 524. ISBN 5458053214. ISBN 9785458053211.
[76] A.A. Chernova, Elementary processes of crystal growth, Phys. Uspekhi 30 (12) (1987) 1098–1100, https://doi.org/10.3367/UFNr.0153.198712f.0678.
[77] S.S. Gorelik, Recrystallization of metals and alloys. Physical Metallurgy, 2005, p. 211.